STRUCTURAL BIOLOGY
ISSN 2059-7983

Fixed target combined with spectral mapping: approaching 100% hit rates for serial crystallography

Saeed Oghbaey,[a]‡ Antoine Sarracini,[a]‡ Helen M. Ginn,[b,c]‡ Olivier Pare-Labrosse,[a] Anling Kuo,[d] Alexander Marx,[e] Sascha W. Epp,[e] Darren A. Sherrell,[c] Bryan T. Eger,[d] Yinpeng Zhong,[e] Rolf Loch,[e] Valerio Mariani,[f] Roberto Alonso-Mori,[g] Silke Nelson,[g] Henrik T. Lemke,[g] Robin L. Owen,[c] Arwen R. Pearson,[h] David I. Stuart,[b,c] Oliver P. Ernst,[d,i] Henrike M. Mueller-Werkmeister[a,d,e] and R. J. Dwayne Miller[a,e,h]*

[a]Department of Physics and Chemistry, University of Toronto, 60 St George Street, Toronto, ON M5S 1A7, Canada, [b]Division of Structural Biology, The Wellcome Trust Centre for Human Genetics, University of Oxford, Roosevelt Drive, Oxford OX3 7BN, England, [c]Diamond Light Source, Harwell Science and Innovation Campus, Didcot OX11 ODE, England, [d]Department of Biochemistry, University of Toronto, 1 King's College Circle, Toronto, Ontario, Canada, [e]Atomically Resolved Dynamics, Max-Planck-Institute for the Structure and Dynamics of Matter, Luruper Chaussee 149, Hamburg, Germany, [f]Center for Free-Electron Laser Science, DESY, 22607 Hamburg, Germany, [g]SLAC National Accelerator Laboratory, 2575 Sand Hill Road, Menlo Park, CA 94025, USA, [h]Hamburg Centre for Ultrafast Imaging, University of Hamburg, Hamburg, Germany, and [i]Department of Molecular Genetics, University of Toronto, 1 King's College Circle, Toronto, ON M5S 1A8, Canada. *Correspondence e-mail: dwayne.miller@mpsd.mpg.de

Received 11 February 2016
Accepted 4 July 2016

Edited by E. F. Garman, University of Oxford, England

‡ These authors contributed equally to this work.

Keywords: femtosecond time-resolved crystallography; high-throughput serial crystallography; fixed-target sample delivery; room-temperature crystallography.

Supporting information: this article has supporting information at journals.iucr.org/d

The advent of ultrafast highly brilliant coherent X-ray free-electron laser sources has driven the development of novel structure-determination approaches for proteins, and promises visualization of protein dynamics on sub-picosecond timescales with full atomic resolution. Significant efforts are being applied to the development of sample-delivery systems that allow these unique sources to be most efficiently exploited for high-throughput serial femtosecond crystallography. Here, the next iteration of a fixed-target crystallography chip designed for rapid and reliable delivery of up to 11 259 protein crystals with high spatial precision is presented. An experimental scheme for predetermining the positions of crystals in the chip by means of *in situ* spectroscopy using a fiducial system for rapid, precise alignment and registration of the crystal positions is presented. This delivers unprecedented performance in serial crystallography experiments at room temperature under atmospheric pressure, giving a raw hit rate approaching 100% with an effective indexing rate of approximately 50%, increasing the efficiency of beam usage and allowing the method to be applied to systems where the number of crystals is limited.

1. Introduction

X-ray diffraction is currently the standard approach for high-resolution structure determination of proteins, and is conventionally carried out at synchrotron light sources. Recent developments in X-ray sources have led to the realisation of hard X-ray free-electron lasers (XFELs). The advantage of these fourth-generation X-ray light sources is their high peak brilliance and improved beam coherence in contrast to synchrotron-generated X-ray radiation. Furthermore, X-rays are generated as short pulses in the 10–100 fs regime, enabling experiments to probe ultrafast chemical and biochemical dynamics (Kern *et al.*, 2014; Tenboer *et al.*, 2015; Barends *et al.*, 2015).

Protein crystallography experiments at XFELs are based on the approach now known as serial femtosecond crystallography (SFX), where the above beam properties allow single

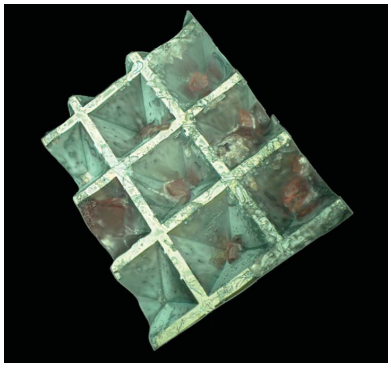

diffraction patterns to be recorded from micrometre-sized protein crystals in a few tens of femtoseconds (Chapman *et al.*, 2011). Using this approach, it is possible to collect a large number of diffracted photons from each protein crystal before the onset of X-ray radiation damage ('diffraction before destruction'; Boutet *et al.*, 2012; Barty *et al.*, 2011). However, a peak brilliance 10^8 times higher than that of a synchrotron source and the short duration of the pulse at an XFEL do result in severe radiation damage to each crystal and make a sample change between each X-ray shot necessary (Barty *et al.*, 2014). This requires either a very large number of small protein crystals or the translation and exposure of multiple regions of larger crystals in order to obtain a sufficient sampling of reciprocal space to allow protein structure determination. Samples must be delivered into the X-ray beam with high spatial precision and, ideally, a sufficient speed/repetition rate to fully use the X-ray beam flux and to avoid misalignment or mistiming in presenting the target to the X-ray beam. Currently, SFX experiments predominantly use variations of a liquid jet (DePonte *et al.*, 2008; Boutet *et al.*, 2012; Sierra *et al.*, 2012), LCP injectors (Weierstall *et al.*, 2014) in vacuum, a grease matrix (Sugahara *et al.*, 2015) or an acoustic injector (Roessler *et al.*, 2016) for sample delivery. In the liquid-jet method, the crystal solution is ejected at high velocity (albeit with a small net volume flow) in a stream onto which, for time-resolved experiments, the pump (laser) and probe (X-ray) pulses are incident. These approaches can support structure determination, but suffer from low hit rates since the random nature of the position of crystals within the jet means that while all X-ray pulses may intersect with the jet, few hit a crystal, wasting photon flux. Even worse for many experiments where crystal production is difficult or expensive, the vast majority of the crystals are wasted, since to maintain the thin flow of crystals the jet velocity needs to be high, increasing the number of crystals which do not intersect an X-ray pulse. The hit rate has been estimated to be as low as one hit per 1600 crystals in some cases (Weierstall *et al.*, 2014). Furthermore, the maximum pressure that the crystals can tolerate before flow-induced damage occurs limits the crystal flow. The flowing stream of sample also adds to the difficulty (compounded by the destructive nature of the X-ray pulse) of taking diffraction reference shots, which would simplify pump–probe experiment data analysis. It is therefore, highly desirable to develop sample-delivery approaches with hit rates that approach 100% and which provide the possibility of recording reference data. For time-resolved studies, the requirement for a high hit rate is particularly acute since sufficient data for structure analysis must be obtained for each and every time point. This significantly increases the volume of sample needed, bearing in mind the high signal to noise required to resolve the very small changes in structure that direct chemical and biological processes or other structural transitions.

Fixed targets provide an attractive solution to the problems described above, and in principle allow the convenient harvesting of crystals and their precise presentation to laser and X-ray beams. Several fixed-target systems have been developed. These include polydimethylsiloxane (PDMS)-based chips (Guha *et al.*, 2012; Lyubimov *et al.*, 2015), in which the crystals sit on the substrate, resulting in noticeable background scatter from the substrate material. An alternate approach utilizes a thin film as a substrate for crystal sample deposition (Hunter *et al.*, 2014; Murray *et al.*, 2015) or patterned silicon substrates (Roedig *et al.*, 2015, 2016) for rapid sample positioning and polycarbonate grids coupled with a goniometer (Baxter *et al.*, 2016; Cohen *et al.*, 2014). Most of these thin-film approaches contribute less background but eliminate the possibility of prior mapping out of crystal positions. The use of a large single crystal as a fixed target has also been implemented (Cohen *et al.*, 2014; Chreifi *et al.*, 2016; Hirata *et al.*, 2014; Keedy *et al.*, 2015; Zhou *et al.*, 2015), but large crystals with the appropriate shape and large accessible surface area and thickness are not easily available for many samples of interest.

We have previously reported a crystallography chip, made by silicon nanofabrication methods (Zarrine-Afsar *et al.*, 2012), for use at microfocus synchrotron beamlines and for time-resolved studies at XFELs that addresses all of the above problems (Mueller *et al.*, 2015). The chip represents a significant improvement over injector schemes, as it requires a smaller amount of sample and effectively minimizes background scatter compared with other fixed-target approaches owing to the removal of excess mother liquor/solvent, a feature that was specifically incorporated into the design of the chip-loading process. The chip contains precisely defined 'features' (pit or well shapes) in which the crystals are trapped. The feature sizes and chip-support layer match the crystal size distribution of the sample under study. The chip structure allows a large number of microcrystals to be loaded, using turbulent fluid flow to introduce random crystal orientations to ensure sufficient sampling of reciprocal space (Mueller *et al.*, 2015). The loaded chip can be mounted on a high-speed translation stage for crystal positioning in the X-ray beam (Sherrell *et al.*, 2015). The accuracy of the nanofabrication process allows precise positioning of the crystals, increasing the hit rate tremendously while keeping sample waste to a minimum, owing to both the relatively high occupancy and the possibility of recovering crystals that were not trapped during the loading process, since all eluent can be collected. The chip also enables the recording of reference diffraction patterns and thus, radiation damage and signal to noise permitting, use of the ratio method for differential detection of the very small early structural changes typically involved in time-resolved studies (Coppens *et al.*, 2009; Mueller *et al.*, 2015). This effectively reduces the volume of data required for structural dynamics studies and further increases the overall efficiency with respect to sample consumption.

In our initial reports the chip could not be operated with the maximum possible hit rate as all features on the chip were probed sequentially, irrespective of the presence or absence of a crystal (Zarrine-Afsar *et al.*, 2012; Mueller *et al.*, 2015). In the present design, we have further improved the chip to reduce multiple crystal instances per loading site, and added a system of fiducial marks for rapid alignment with well defined

reference points and quick identification of chip compartments. The fiducial system enables error-free position determination and identification of each crystal in the array. Finally, we have developed a high-speed single-crystal spectrometer to map the crystal positions prior to the diffraction experiment. High-speed mapping is important for crystals with finite lifetimes once mounted, and increases hit rates substantially as only features containing crystals are sampled at the beamline.

As a proof of principle, we demonstrate here that this chip concept, with a fiducial system and mapping protocol, can achieve a raw hit rate of up to 85%. When inherent variations in crystal quality as well as intensity fluctuations owing to the SASE profile of the XFEL beam are taken into account, this approaches the maximum achievable sampling efficiency. Furthermore, the method facilitates a data-collection rate that comes close to the fully optimized use of the XFEL X-ray flux with low sample consumption, thus opening up the study of precious protein systems. Specifically, we demonstrate the efficacy of the chip concept using carboxymyoglobin, as a prelude to femtosecond time-resolved studies of ligand dissociation from the haem binding site.

2. Materials and methods

2.1. Nanofabrication

The chip is made out of a single-side polished silicon wafer (WRS material) with a thickness of 550 µm coated with 50 nm low-pressure chemical vapour-deposition (LPCVD) silicon nitride, applied as an etching mask for KOH etching. Conventional lithography is utilized to transfer the photomask pattern onto an organic photoresist (Shiply S1818), which is spin-coated onto the silicon wafer. After exposure to UV light, the pattern is developed and cleaned. In the next step, the silicon nitride under the photoresist is etched away using SF_6 plasma reactive-ion etching. The photoresist is used in the plasma-etching stage as an etch mask and must be stripped away afterwards. The wafer is then placed in a supersaturated aqueous KOH solution [40%(*w*/*w*)] at 80°C to etch away bulk silicon until the desired feature depth is reached. A similar process is carried out for developing the back-side features until the desired hole size is reached. The fabrication process is shown in Fig. 1. The wafer is then cleaned using a standardized cleaning process with a solution consisting of H_2O_2:NH_4OH:H_2O in a ratio of 1:1:5 by volume at 70°C, which leaves the chip surface hydrophilic. Finally, the wafer is separated into individual chips by dicing.

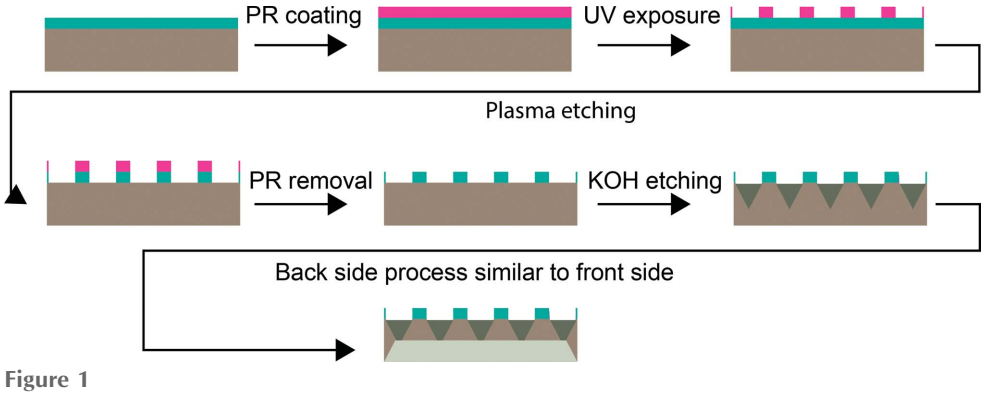

Figure 1
Fabrication scheme for the crystallography chip. The process starts with conventional UV lithography to transfer the pattern of loading sites to a silicon wafer [grey, with a layer of silicon nitride (SiN) in cyan] coated with photoresist (pink). The pattern is then transferred to the SiN layer using reactive-ion etching and the photoresist is stripped. The SiN layer plays the role of the mask for wet etching in the subsequent steps. KOH etching results in a trapezoidal shape that enhances loading efficiency. The same procedure is repeated for the back side of the chip using a different photomask to make it thin enough to fit a specific size of crystals.

2.2. Protein expression, purification and crystallization

2.2.1. Sperm whale myoglobin expression and purification. The sperm whale (*Physeter catodon*) myoglobin (SWMb) expression plasmid (pMb413a) with a D122N mutation was kindly provided by Professor John S. Olson (Rice University, USA) and the protein was expressed constitutively in *Escherichia coli* BL21(DE3) cells at 37°C for 3 days. SWMb with bound carbon monoxide (SWMb–CO) was purified as described previously, with some modifications (Springer & Sligar, 1987; Mueller *et al.*, 2015). Briefly, (i) all buffers used in purification were saturated with CO gas at 1 atm; (ii) after ammonium sulfate precipitation, the collected precipitant was dissolved in a small volume of 20 m*M* sodium phosphate pH 6.0 and dialyzed overnight against this buffer; (iii) the dialyzed protein was concentrated and applied onto a CM Sepharose (GE Healthcare Life Sciences) fast flow column which had been pre-equilibrated with the same buffer and a linear pH gradient of 20 m*M* sodium phosphate pH 6.0 to 50 m*M* sodium phosphate pH 9.0 was used for elution; (iv) eluted protein fractions were concentrated and applied onto a Superdex 75 gel-filtration column (GE Healthcare Life Sciences) in 20 m*M* Tris–HCl, 150 m*M* NaCl buffer pH 8.0 to remove aggregates; (v) the peak fractions were combined, solid sodium dithionite was added (20 m*M* final concentration) and, after 10 min incubation, the protein was rapidly applied onto a Sephadex G-25 column equilibrated with 10 m*M* Tris–HCl buffer pH 9.0 under 1 atm of CO (Li *et al.*, 1994). The eluate containing SWMb–CO was concentrated for crystallization.

2.2.2. SWMb–CO crystallization. To ensure that the SWMb crystals were grown in the reduced CO-bound form, the crystallization buffers were saturated with CO gas. The SWMb–CO crystals were grown in 3 ml Monoject blood collection tubes (Covidien, Mansfield, Massachusetts, USA) prefilled with CO gas at 1 atm. 180–200 µl crystallization solution containing 50–60 mg ml^{-1} protein in 10 m*M* Tris–HCl pH 9.0, 2.5–2.6 *M* ammonium sulfate was added to the Monoject tubes. Seeding was used to promote the nucleation of

large numbers of small crystals. The SWMb–CO crystals were crushed in 10 m*M* Tris–HCl pH 9.0, 3.2 *M* ammonium sulfate. The seeds were diluted 1:100 under the same buffer conditions and 10 µl was added to each tube. The size distribution of the final crystals was controlled by adding 180 µl 10 m*M* Tris–HCl pH 9.0, 3.2 m*M* ammonium sulfate pre-saturated with CO gas to each tube after crystals appeared. This method produces crystals of appropriate sizes, corresponding to the chip parameters, as described previously (Mueller *et al.*, 2015). Crystals were loaded onto the chip as shown in Fig. 2. To prevent salt-crystal formation, all experiments for chip loading were performed in a portable glove bag (Sigma–Aldrich) at a temperature of 24°C and a humidity of 60%.

2.3. *In situ* microspectrometer

A fibre-coupled microfocus absorption spectroscopy setup for sample characterization and chip mapping was developed (adapted from Kirchner *et al.*, 2014). The setup utilizes a fibre-coupled broadband light source, off-axis parabolic mirrors, a fibre-coupled USB spectrometer and a three-axis translation stage (SmarAct) for accurate sample positioning (similar to the beamline end station described in Sherrell *et al.*, 2015).

A deuterium–halogen lamp (Ocean Optics; 215–2500 nm) or an LED lamp (Ocean Optics; 425–650 nm) was used as a fibre-coupled light source. The light source is coupled to a 200 µm core diameter fibre. The first off-axis parabolic mirror (OPAM) collimates and reflects the light by 90° onto a second OPAM with half the effective focal length of the first. This mirror focuses the light onto the sample. These two mirrors constitute an all-reflective 2:1 microscope, resulting in a focal spot size of nominally 100 µm at the sample. A third OPAM collimates the transmitted light onto a fourth OPAM that focuses the light into a fibre-coupled USB spectrometer sensitive to light in the wavelength range 200–850 nm (Ocean Optics; USB2000-UV-VIS). Absorption spectra were generated by taking the logarithm of the background-subtracted transmission spectra divided by the light-source spectrum.

The parabolic mirror pairs are placed in a rigid four-bar optical cage system (Thorlabs; Fig. 3*a*) using a custom-designed mount, which fixes the rotation of the mirrors. This ensures very easy and precise alignment, which does not need to be adjusted. A CMOS camera (Thorlabs) and a close-focus zoom lens (Edmond Optics), with a minimum field of view of approximately 6 mm and a large working distance, is used as an off-axis viewing system for chip alignment.

2.4. SFX data collection

X-ray data collection was performed at the XPP instrument at LCLS at room temperature with an X-ray beam size of 20 × 20 µm and 10^{10} X-ray photons per pulse with a photon energy of 9.58 keV and a nominal sample-to-detector distance of 67.8 mm under proposal LF70. A diamond (111) monochromator was used, resulting in a narrow bandwidth: $(\Delta E/E) = 5 \times 10^{-5}$. The diffraction data-collection rate was 10 Hz, which was limited by the detector-readout speed. Data were recorded using a Rayonix MX170-HS CCD detector.

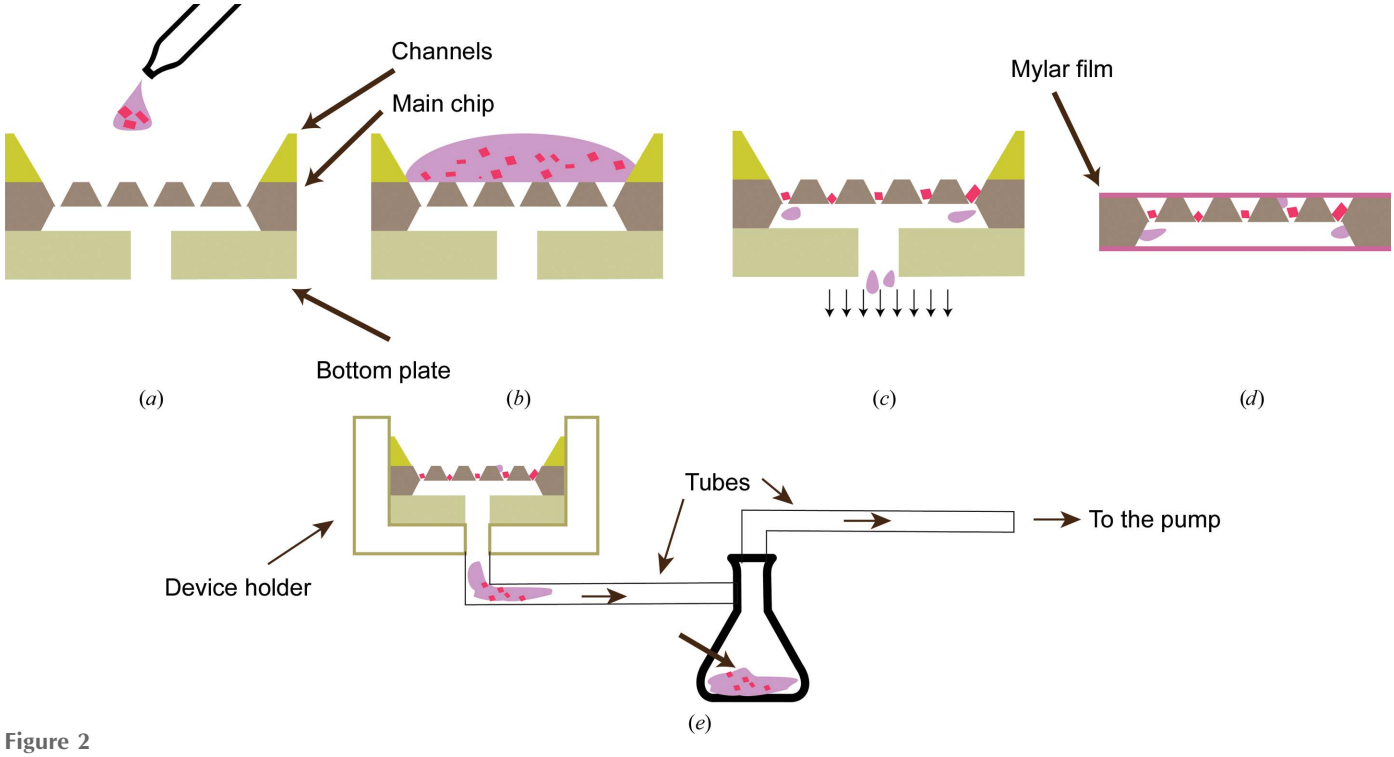

Figure 2
(*a*, *b*, *c*) Chip-loading scheme with chip components designed for crystal solution loading. The silicon piece with channels in it is placed on top of the chip to guide crystal solution into the compartment rows. The bottom plate helps to apply effective negative pressure to trap the crystals in features (*c*). (*d*) The loaded chip is wrapped in a thin film of Mylar to avoid crystal dehydration. The crystal solution removed from the chip can be collected in an additional reservoir for use with a different chip size (*e*). All figures are schematics and are not to scale.

In the manner described previously (Mueller *et al.*, 2015), data collection was organized such that ten shots of the XFEL were integrated into a single frame of the detector, providing the reference or 'before' image, and in a second step a single shot of the same crystal was recorded. In a pump–probe experiment, this second image would be the only one with a possible pump interaction. We note that the first image integrated from ten individual XFEL shots was recorded with a beam attenuated roughly 30 times after the monochromator, ensuring that radiation damage is below the detection threshold. The total absorbed X-ray dose per crystal was 5.7 kGy for the sum of ten attenuated pulses plus 16.8 kGy without the attenuator, using a 480 µm sapphire attenuator. These values were calculated using the *RADDOSE-3D* software suite (Zeldin *et al.*, 2013), ignoring the effect of photoelectron escape. These are well below the damage threshold (Garman limit) at which noticeable spectroscopic changes are observed as determined in previous studies (Owen *et al.*, 2011). A broadly accepted rule of thumb in macromolecular crystallography is that a structural change of less than 20% does not contribute significantly to the final electron density (Pearson *et al.*, 2007; see the Supporting Information for safe-dose calculation).

2.5. Data analysis

Individual images were extracted from the XTC streams and stored in HDF5 format for indexing with *Cheetah* and *indexamajig* (*CrystFEL*; White *et al.*, 2012). From the output of *indexamajig*, information was extracted to calculate both raw hit rates ($h_{\rm raw}$) and fractions of indexed images ($h_{\rm idx}$). A spot search was carried out on these extracted images using the *DIALS* spot-finding routine (Waterman *et al.*, 2016), which is based on the *XDS* algorithm (Kabsch, 2010). For integration, data merging and structure determination, with an improved method based on post-refinement and partiality correction (Ginn, Brewster *et al.*, 2015), images were indexed using the *TakeTwo* (Ginn, Roedig *et al.*, 2016) algorithm in *cppxfel* (Ginn, Evans *et al.*, 2016) and integrated using simple summation, with an integration box with a 5 × 5 foreground,

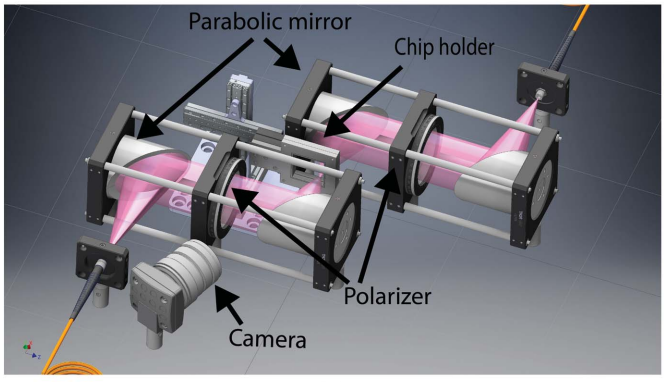

(*a*)

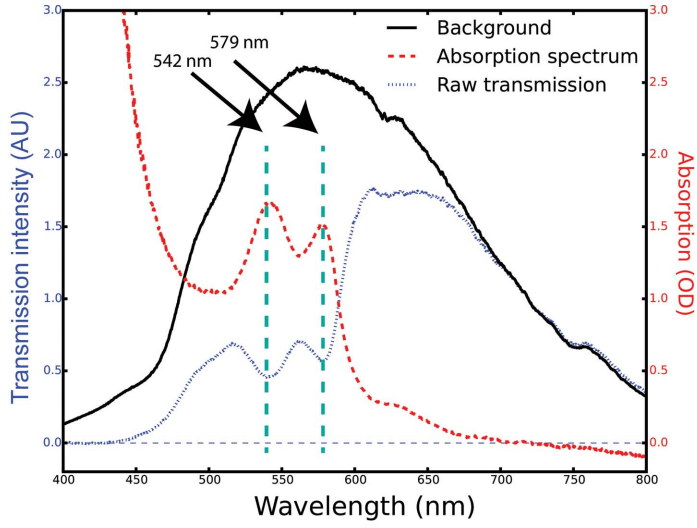

(*b*)

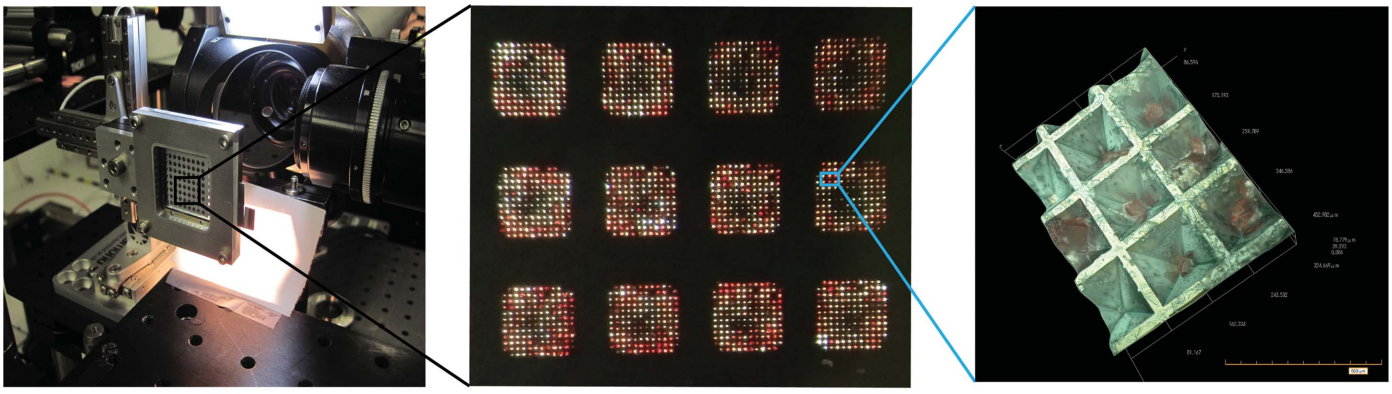

(*c*) (*d*) (*e*)

Figure 3
(*a*) Schematic representation of the high-speed spectroscopy setup for mapping the loaded chip. (*b*) Example spectrum of a carboxymyoglobin crystal recorded from a crystal-containing feature. The characteristic absorption bands for carboxymyoglobin (542 and 579 nm; Springer & Sligar, 1987) are indicated. (*c*) The chip mounted in the beam at the XPP instrument at LCLS. (*d*) A magnified picture of chip compartments loaded with crystals. The carboxymyoglobin crystals can be easily identified owing to their red colour. (*e*) Three-dimensional image of crystals trapped inside a feature (image taken using a Hirox RH2000 microscope as part of user facilities on site at SACLA, RIKEN, Japan).

Table 1
Refinement statistics.

Resolution range (Å)	42.26–1.90
Completeness (%)	100
R_{work}/R_{free} (%)	21.1/26.0
No. of non-H atoms	
Protein	1225
Sulfate	1
Water	20
R.m.s. deviations	
Bonds (Å)	0.016
Angles (°)	1.8
Ramachandran plot	
Most favoured (%)	96.7
Allowed (%)	3.3

one-pixel buffer and two layers of additional surrounding pixels for background subtraction. The detector distance was refined to 68.6 mm and the wavelength to 1.293 Å, in contrast to the values of 67.8 mm and 1.312 Å, respectively, which were recorded during beam time. Crystal orientations were initially refined according to a previous protocol to minimize the spread of Ewald spheres on which the reflections are observed (Ginn, Messerschmidt *et al.*, 2015), with additional refinement of the three unit-cell dimensions for the orthorhombic space group. These positions were integrated, according to the chosen shoebox, and the potential reflection was classed as a 'strong' reflection if it had an integrated intensity of 32 counts or greater. Post-refinement was carried out against a reference data set according to a previous protocol (Ginn, Brewster *et al.*, 2015) using a binary partiality of 0 or 1. A partiality of 1 is assigned to reflections for which the conventionally calculated partiality is 0.2 or greater and 0 if this is not the case. Only one cycle of post-refinement was performed after an initial Monte Carlo merge in order to refine which reflections were included and excluded in the merge, but partiality correction on these data was found to be unstable, likely owing to the monochromatic beam. The reference data set was generated by an initial merge of the images and was used to post-refine individual images to improve the merging statistics R_{split} and $CC_{1/2}$. The bandwidth for refinement was set to 0.01% of the pulse wavelength and the mosaicity to 0.04°, leading to around 166 accepted reflections per image. Images were rejected if they were below a correlation threshold of 0.8 and individual reflections were rejected beyond 1.8 standard deviations from the mean of all observation intensities for a given reflection (parameters as defined in Ginn, Brewster *et al.*, 2015). Linear scale factors were applied to each image during merging to best match the reference density. Intensities were converted to amplitudes using *TRUNCATE* (Winn *et al.*, 2011). The protein and haem group from the sperm whale myoglobin structure (PDB entry 1vxa; Yang & Phillips, 1996) were used as a starting model for molecular replacement using *Phaser* (McCoy *et al.*, 2007). Building and refinement were performed using *Coot* (Emsley *et al.*, 2010) and *REFMAC*5 (Murshudov *et al.*, 2011). Following the placement of waters and a single sulfate atom, carbon monoxide was built into the density and refined (Fig. 4*b*). Refinement statistics are presented in Table 1. Coordinates and structure factors for the *P. macrocephalus* myoglobin with carbon monoxide covalently bound have been deposited in the Protein Data Bank with accession code 5jom.

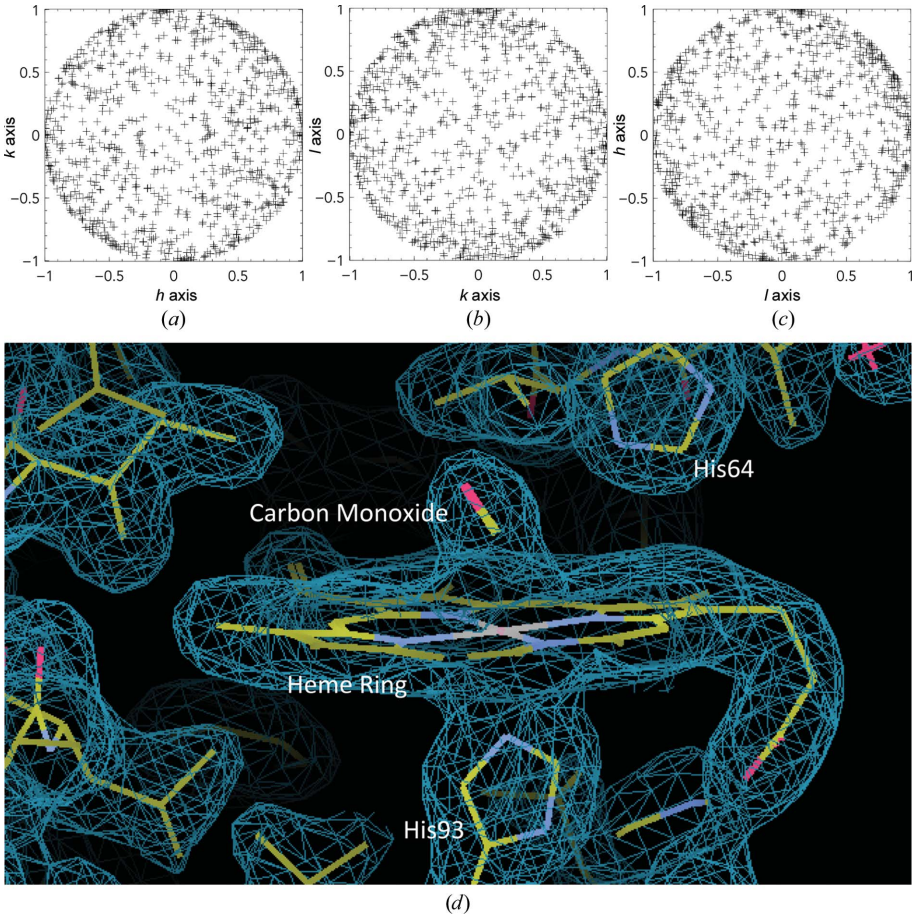

Figure 4
(*a*) A (1, 0, 0) vector was multiplied by each crystal orientation matrix and its associated symmetry operations. The data for each pair of axes are plotted against each other, showing a uniform sampling of crystal orientation. (*b*) Representative electron density at 1.9 Å resolution, contoured at 1σ, for carbon monoxide (CO) bound to the haem iron of sperm whale (*P. macrocephalus*) myoglobin generated from data collected using the crystallography chip.

3. Results

3.1. Chip design

The crystallography chip is a microfabricated 28 × 28 mm silicon substrate consisting of compartments with features designed specifically for trapping micrometre-sized crystals. The current design is comprised of 9 × 9 compartments, where each

compartment contains an array of 12 × 12 features (Fig. 5), resulting in 11 664 positions on the chip, 11 259 of which are for trapping crystals. Each feature is square-shaped with a 100 µm wide top aperture and a bottom aperture size ranging in width from 5 to 30 µm.

A key characteristic of the etched pattern on the silicon wafer is the trapezoidal geometry resulting from anisotropic etching of the different silicon crystal planes (Seidel *et al.*, 1990). The aperture and depth of the resulting features can be optimized to match the average crystal size of the system of interest. The opening at the bottom of each feature allows the removal of excess solution to recover any untrapped smaller crystals and to remove as much of the mother liquor remaining from the loading process as possible, dramatically reducing unwanted background scatter.

The thin regions of the chip designed for crystal trapping are easily deformable and, if not supported, can flex during loading and translation, resulting in a loss of positioning accuracy. The chip therefore includes thick silicon spacer bars between compartments to increase rigidity (Figs. 5*a* and 5*b*).

It should be noted that the thickness of the raw silicon wafer varies by 10 µm, which affects the final feature sizes and the etching rate at the extremities of the individual compartments and the chip itself. The etching is slightly slower at the edge of the chip than in the centre. This leads to a radial distribution of feature sizes of about 5 µm over each individual compartment and over the whole chip. This non-uniformity means that a small number of features on the outermost part of the chip might not be fully open at the bottom and thus cannot hold a crystal. Nonetheless, this geometry and method of fabrication result in a chip capable of trapping single crystals. The method of fabrication can be improved and easily scaled and thus allows the adjustment of the number of compartments and features to further increase the chip capacity if desired.

Each compartment has five fiducials, three of which are at the corners for alignment and two additional ones serving as unique addresses, allowing the precise and unambiguous positioning of every feature on the chip. The fiducial marks are designed to enable alignment of the chip using an inline imaging system with minimum aberrations to locate the centroid of the fiducial mark. The fiducial marks have a length of 100 µm and width of 10 µm and are in the form of a double cross or '#' symbol to facilitate automated image analysis (Figs. 5*c* and 5*d*). The '#' reduces edge confusion in the image-processing/alignment algorithm, hence reducing the number of false-positive matches. In principle, the corner features of every compartment could be used as intrinsic fiducial marks, but as the feature dimensions have some irregularity, owing to the silicon processing, this is less reliable.

3.2. Chip loading

Two auxiliary parts have been fabricated for use in the loading process to improve its ease and efficiency (Fig. 2). The first is an extremely flat silicon 'bottom plate' (<5 nm surface roughness over the whole contact area) with a hole through it, which lies underneath the crystallography chip. This very smooth surface provides a good seal for a closed-flow system to direct the crystals through the features to trap the crystals. The second is a silicon chip with nine linear channels etched across it, which span the length of the chip and with widths matching the size of one compartment. This part sits on top of the crystallography chip to direct the flow of liquid during sample loading, reducing sample waste by minimizing flow over dead space on the chip and maximizing the flow rate over the features. This avoids the adsorption of crystals on to the chip at locations where they would not be sampled in the diffraction experiment. The whole assembly is stacked and held together accurately using a custom holder.

To minimize stress on the crystals, the loading process is performed at a controlled temperature to match that of crystallization, and at controlled humidity to prevent salt-crystal formation from the mother liquor (see §2 for details). First the crystals, in their mother liquor, are dispensed onto the chip using a pipette, using siliconated tips to minimize sticking of crystals to the pipette tip. Depending on the crystal density, volumes of 60–80 µl crystal slurry are sufficient to load a chip with approximately 40% occupancy. Negative pressure is applied to the underside of the chip and the solution is sucked through the features, leaving the crystals trapped

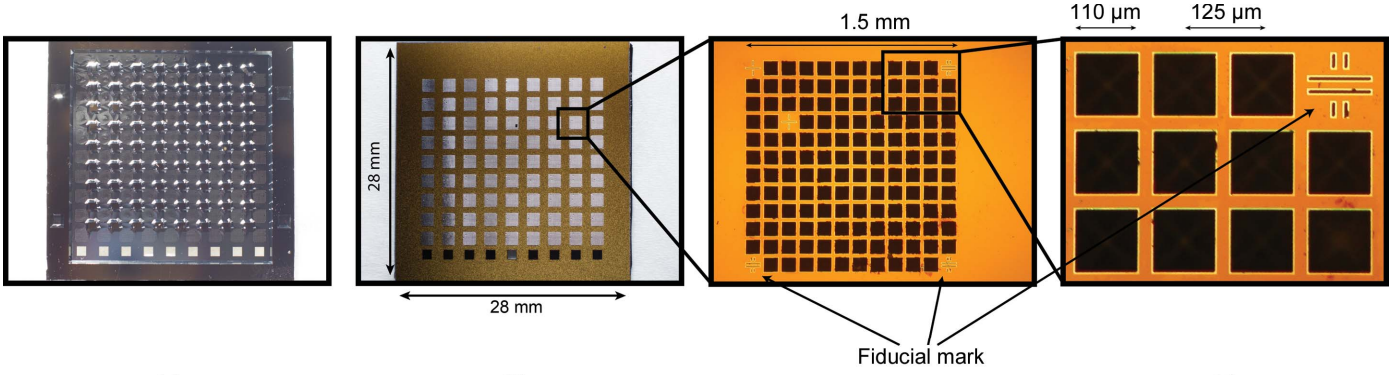

Figure 5
Back (*a*) and front (*b*) of the chip and a close-up view of an individual compartment (*c*). Each chip comprises 9 × 9 compartments with 12 × 12 features per compartment. As each feature is designed to hold a single crystal, the maximum capacity of the chip is 11 259 (139 × 81) crystals (based on 144 features minus five fiducials per compartment). (*d*) Magnified portion of a compartment showing the crystal-trapping features and a fiducial mark.

inside a feature with a minimal volume of mother liquor. The etched away area on the back side of the chip creates a large evacuated volume for efficient removal of the mother liquor (Fig. 2*c*). The amount of negative pressure applied during the loading process needs to be carefully adjusted. Too much suction dehydrates the protein crystals too quickly, while too little suction leaves excess mother liquor on the surface of the chip, resulting in increased background scatter. To avoid the formation of salt crystals, adjusting the suction and humidity is important when high salt concentrations are used as precipitant. Next, the chip is removed from the closed-flow system and rapidly sealed with 4 µm thick Mylar film on each side. Finally, the chip is placed in a custom holder, which is specially designed to accommodate the two 4 µm films of stretched Mylar and the chip.

The permeability of the Mylar film is low enough to minimize protein dehydration and maintain the crystals in a humid environment long enough for data collection. The Mylar introduces some diffuse background to the diffraction pattern (see Fig. 6), which is subtracted during the standard data-processing procedures. The bottom hole of the feature acts as an aperture which helps to remove background scatter (see Fig. 6). In the future other, lower-scatter, polymer films or 30–50 nm SiN films could be substituted to significantly further reduce the background scatter. In addition, the silicon nitride and etched silicon surfaces, which are usually covered with their native oxides, are very hydrophilic, and therefore it may be possible to improve the loading efficiencies and removal of excess mother liquor by reducing the hydrophilicity of the chip using simple surface treatments.

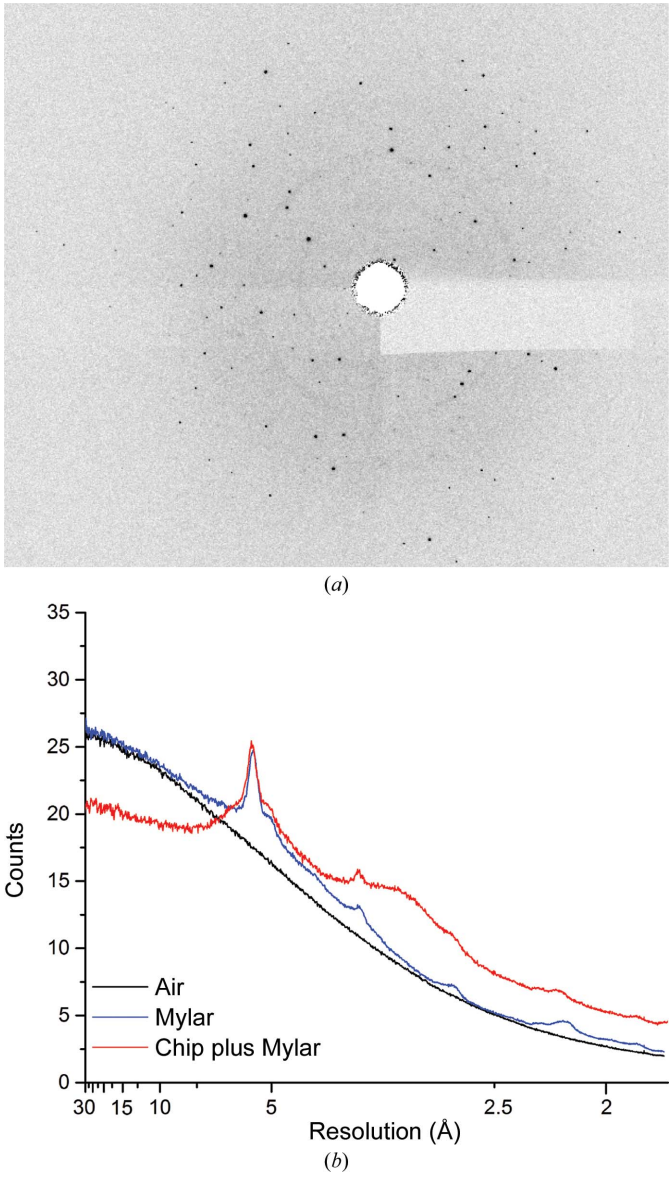

Figure 6
(*a*) Example of diffraction image with Mylar background (image obtained at the XPP endstation at LCLS), (*b*) comparison of diffuse scatter of air, air plus Mylar and a loaded chip (empty feature) as a function of resolution. The feature acts as an aperture, reducing the background at low resolution (data obtained on beamline I24 at Diamond Light Source).

3.3. Optical spectroscopy setup

To increase the hit rate, we have developed a high-speed UV–Vis microspectrometer (adapted from Kirchner *et al.*, 2014) with a focus spot size of 100 µm and that is sensitive to a wavelength range of 215–850 nm to map crystal positions in the chip. Transmission spectra are recorded from each feature to determine whether or not it harbours a crystal. This information can subsequently be passed to the beamline data-acquisition software so that empty features are not addressed during the SFX experiment. This approach also allows differentiation of protein and salt crystals, as salt crystals strongly scatter the light and can therefore be easily identified. The rapid filling of the chip relative to the rate of salt-crystal formation greatly reduces the growth of salt crystals during chip loading (§3.2). However, for salt-based crystallization conditions, some features can still be occupied with salt crystals and, in addition, salt crystals can grow on protein crystal surfaces.

To ensure complete compatibility between the chip mapping and positioning of the chip at the X-ray beamline, we use identical precision translation stages for the spectroscopy/mapping and for the X-ray beamline and the same coordinate-system transform to convert feature positions into translation-stage motions as described previously (Sherrell *et al.*, 2015). Once mounted, the chip is translated along the spectroscopy probe beam axis until it is at the beam focus and the optical spot size is minimized. Compensation is made for chip tilt in the coordinate-system transform based on the position of the three outermost corner fiducial marks on the chip. The chip is then translated successively to each feature, where a spectrum is recorded and named according to the feature address as defined by the coordinate system. The experimental setup is shown schematically in Fig. 3(*a*), together with representative spectra of carboxymyoglobin crystals recorded from the chip (Fig. 3*b*). The time needed to acquire a spectrum with acceptable signal to noise limits the speed at which a chip can be scanned. In the experiments reported here the integration time for recording each feature spectrum was 250 ms, resulting

Table 2
Hit-rate statistics for mapped chips.

Chip No.	1	2	3	4	5	6	Average (%)
Positive spectra	6983	2237	9174	4325	8618	3782	52† (fill factor)
Maximum No. of diffraction images possible‡	4467	1485	5993	3100	6064	2609	57
Diffraction images with >10 peaks	4093	1432	5298	2790	4161	2148	84 (h_{raw})
Indexed images	1802	825	2479	1611	2863	1171	46 (h_{idx})

† The number of features with a verified spectrum of carboxymyoglobin. ‡ The maximum expected number of diffraction images taking empty (negligible amplitude) X-ray pulses into account.

in a 40 min acquisition time for a whole chip map. However, improvements in integration time and the use of an external trigger have since been implemented, leading to an acquisition time of approximately 8 min per chip.

After the chip has been fully scanned, the background-corrected transmission spectra are processed to determine the loaded feature positions. This is performed by taking the ratio of the integral of a part of the transmission spectrum which is expected to show significant absorption (500–700 nm for carboxymyoglobin) in comparison to the integral of a part of the spectrum where there is little absorption (700–850 nm). A feature is marked as containing a crystal if the resulting number is below the threshold ratio of an empty feature. A list is then generated containing each feature address and a binary value corresponding to whether or not the feature contains a crystal. This scheme is very fast and is generally effective, but suffers from a few drawbacks. Firstly, the effectiveness of the asymmetric filter described above depends on the specific absorption spectrum of the sample. Secondly, it is impossible, based on the spectroscopic data alone, to distinguish crystalline sample from amorphous sample. Subsequent diffraction data showed that 15% of features marked as containing a crystal did not yield Bragg peaks, indicating the presence of amorphous material in our crystal preparation. Nonetheless, we were able to consistently achieve 85% raw hit rates using the XPP instrument at LCLS (Chollet *et al.*, 2015; §3.4). It is possible that a more robust way of correlating the spectral signal with that of crystalline protein can be found to increase the hit rate; however, there is likely to be some residual crystal-to-crystal variation in diffraction quality that will preclude reaching hit rates of exactly 100%. Nevertheless, the present hit rate already allows the highly efficient use of the current XFEL pulse stream.

3.4. Data acquisition and analysis

For a proof of principle, we investigated the use of the crystallography chip with spectroscopic mapping during an experiment using the XPP instrument at the Linac Coherent Light Source (LCLS), determining the structure of carboxymyoglobin using the SFX approach. Spectroscopic mapping was carried out on six chips, which then underwent X-ray data collection. The use of a monochromator resulted in $\sim 10^{10}$ photons per image, which was considerably fewer than the 10^{12} photons per image typical in an SFX experiment. For this reason, in a typical 'full-throttle' experiment, we would expect a useful data set to be collected from substantially fewer images, with the expected attendant improvements in signal to noise with more diffracted X-ray photons. The average number of X-ray hits recorded for a scanned chip was around 5000 (Table 2). Here, an X-ray hit is defined as an image containing >10 intensity maxima, as determined by a fast peak search using *OnDA* (Mariani *et al.*, 2016), which we report here as raw hit rates (h_{raw}). This indicates that the crystal loading efficiency on the chip was approximately 50%. The use of a shot list based on the spectroscopic chip mapping resulted in an actual overall hit rate of greater than 85%.

A quantity that describes the success rate of diffraction events more reliably is the fraction of shots that lead to indexable diffraction patterns, h_{idx}, which is available after data reduction and indexing of the entire data set. The 'indexable hit rate' h_{idx} can never be higher than h_{raw}, and will usually be considerably lower, as not every crystal diffraction pattern can be indexed. Obviously h_{idx} depends not only on the efficiency of sample delivery, but also on the type and quality of the crystals and on the performance of the indexing software. Utilizing *CrystFEL* to index the diffraction data gives an h_{idx} of 43%, which represents on average 2000 successfully indexed images per chip. Finally, because of the stochastic nature of X-ray pulse generation, there is a shot-to-shot variation in both pulse intensity and spectral distribution. In our experiments an X-ray monochromator was used. As a consequence, the natural variation in the X-ray pulse intensity leads to a significant fraction of 'empty' pulses. As a result, even features containing a 'good' crystal may not result in a 'hit'. To take this into account, corrected hit rates, h'_{raw} and h'_{idx}, were calculated on the basis of the number of X-ray pulses observed with intensity greater than a certain threshold. This correction leads to an increase in the h_{idx} rates to 46%, *i.e.* close to 50% indexable diffraction patterns. The total number of diffraction images (>10 peaks, h_{raw}) collected from the six chips was of the order of 20 000, of which half resulted in successfully indexed diffraction patterns (Table 2, the exact number is 10 751). Not all of these images were used in final structure determination (see Table 1 and §2).

The dimensions of the crystals that were successfully indexed were 20 × 20 × 40–70 µm. Analysis of the orientation matrices (Fig. 4*a*) confirms that the crystals are reasonably randomly oriented, with no evidence of preferred alignment within the chip features. The quality of the intensities derived by the application of *cppxfel* (Ginn, Brewster *et al.*, 2015) was reasonable (Table 3), despite the heavy attenuation of the XFEL pulses (see §2). The *TakeTwo* algorithm within *cppxfel* increased the indexing rates to approximately 100% of images which registered more than 20 spots using *DIALS* spot finding (Waterman *et al.*, 2016). These data, when merged (with *cppxfel*), yielded a complete data set and supported model building and refinement to obtain a high-resolution model capable of supporting the analysis of small conformational changes. Table 1 summarizes the refinement statistics and

Table 3
Data collection and processing.

Values in parentheses are for the highest resolution shell.

Diffraction source	LCLS XFEL source, XPP endstation
Wavelength (Å)	1.29
Temperature (K)	293
Detector	Rayonix MX170-HS CCD
Crystal-to-detector distance (mm)	340
Exposure time per image (s)	0.1
Space group	$P2_12_12_1$
a, b, c (Å)	38.13, 46.48, 84.52
α, β, γ (°)	90, 90, 90
Resolution range (Å)	33.43–1.90 (1.93–1.90)
Images merged	8957
No. of unique reflections	12354
Completeness (%)	100
$\langle I/\sigma(I)\rangle$	6.0
Multiplicity	51.6
$R_{\rm split}$ (%)	10.1 (46.1)
Matthews coefficient $V_{\rm M}$ (Å^3 Da^{-1})	2.18
Solvent content $V_{\rm s}$ (%)	43.5
Observations per image to edge of detector	166 ± 28
$CC_{1/2}$ (%)	99.6 (42.6)

Fig. 4(*b*) shows a representative portion of the electron-density map.

4. Discussion

The batch process for chip fabrication makes it possible to produce many chips at once. The tunability of the fabrication process enables the development of different-sized features to accommodate a range of crystal sizes up to hundreds of micrometres. This makes the crystallography chip well suited for a large range of crystalline protein samples down to dimensions of a few micrometres. This aspect of the chip is especially important for SFX experiments and the study of proteins for which large crystals are difficult to obtain. In addition, owing to the well shaped features, the loading leads to centred crystals, ensuring that the X-ray beam hits the centre of the crystal rather than an edge.

The minimal amount of mother liquor around each crystal and the thin Mylar 'windows' result in very low background, making the chip an attractive alternative compared with other sample-delivery methods such as the liquid jet and LCP injectors, where the mother liquor or LCP carrier introduces significant background scatter to the diffraction data. An additional advantage of the silicon-based chip is that it can be cleaned and reused. Finally, we have not observed any evidence of radiation damage to the chip itself at either microfocus synchrotron beamlines or when exposed to an XFEL beam.

One of the greatest advantages of the fixed-target chip, in combination with spectroscopic mapping, is the ability to define a spatial address for each protein crystal located in the chip and thus extract the corresponding data selectively for a particular sample. This provides the possibility of performing additional diagnostics with the potential to improve SFX analysis, for example post-sorting of diffraction data based on optical absorption. In general, any measurable characteristic of an individual crystal can be recorded and referenced later for data analysis.

Another application of the optical spectroscopy setup is *in situ* sample characterization. Unstable samples that require sealing from the atmosphere or specific ambient conditions can be tested for longevity, for example in the case of carboxymyoglobin the ligand-binding state can be monitored for each individual crystal. In addition, chips can be scanned before and after X-ray exposure to observe the extent of X-ray-induced and laser-induced damage (in case of time-resolved SFX experiments). This is important as femtosecond time-resolved experiments generally involve very small structural changes and thus there is a need to go to the maximum photoexcitation possible to ensure the majority of molecules in the crystal are reacting. This requires laser powers that are typically right at the limits of multiphoton processes unrelated to the photophysics and photochemistry of interest. This capability allows spectroscopic analysis to ensure proper excitation conditions below this limit and the onset of X-ray damage.

The improved jet-based sample-delivery system utilizing LCP media has reported hit rates around 8% with an indexing success rate within this subset of images of 22%, resulting in an overall successful $h_{\rm idx}$ rate of about 1.6% (Weierstall *et al.*, 2014). Even allowing for possible differences in crystal quality, the hit rates achieved with this chip constitute an improvement of at least an order of magnitude over competing methods. The improved percentage of successfully indexed shots is owing to a combination of reduced background scatter with the chip (see unmapped hit rates; Fig. 7) with a further gain in efficiency owing to spectroscopic mapping (Table 2 and Fig. 7). Differential polarization analysis, using a simple polarizer between the sample and detector in the microspectrometer, or second-harmonic generation-based imaging to distinguish amorphous and crystalline protein will further improve this correlation to close to the 100% $h_{\rm raw}$ limit.

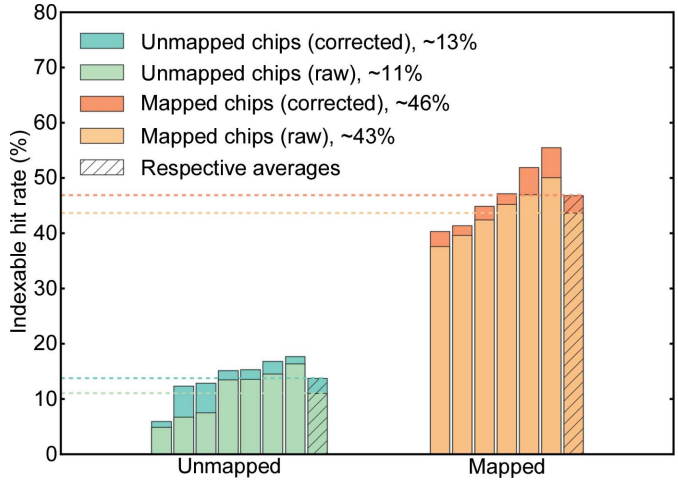

Figure 7
Percentage of indexed diffraction patterns for unmapped (left) and mapped (right) chips: light colours, without correction for missing X-ray pulses; dark colours, after correction. Mapping the chip improves the success rate approximately threefold.

With improvements in post-refinement (using a modified approach based on Ginn, Brewster *et al.*, 2015), we find 8957 indexable diffraction patterns to be sufficient to obtain a structure from monochromatic XFEL data. This means that in principle, with improved spectral mapping (including the differentiation between crystalline and amorphous material) *and* if optimal loading is achieved (>50%), one or two chips could provide sufficient diffraction data for structure determination (ultimately depending on the diffraction quality and the parameters of the crystal such as the space group). Data collection at XFELs is currently limited in principle by the repetition rate of the FEL (120 Hz for LCLS in the US, 30 Hz for SACLA in Japan), but practically by the repetition rate of the available detectors. At the XPP instrument, the Rayonix detector used in these experiments runs at 10 Hz. Taking into account the mounting and alignment time, this would mean sufficient data for *de novo* structure determination could be collected within less than 20 min. For the chips described (feature spacing of 125 µm), the present translation-stage system is capable of scanning at 107 Hz using the current approach of pausing at each feature for laser/X-ray exposure.

Larger data sets will, of course, improve the overall signal-to-noise ratio, and 20 000 useful diffraction patterns could, in principle, be acquired at 100 Hz from an optimally loaded and mapped chip containing a larger number of features in less than 4 min. For time-resolved studies, this would mean that a full time series with up to 100 time points could be collected within a few hours. This would enable multiple systems to be studied for comparative studies of structural dynamics or studies over many decades in time in a single experimental visit to capture more fully relevant dynamics.

5. Conclusion

We present an improvement of a chip-based approach to sample delivery for SFX (an extension of Mueller *et al.*, 2015; Zarrine-Afsar *et al.*, 2012), which combines spectroscopic mapping of crystal positions with an innovative low-background fixed target to provide a versatile and highly efficient system with significant advantages over other sample-delivery methods. In its current version, the chip is designed for time-resolved SFX experiments, but it can be used at virtually any synchrotron or XFEL beamline in combination with the dedicated mini endstation (Sherrell *et al.*, 2015). The efficient process of loading and handling samples, in combination with spectral mapping, significantly increases the productive data-acquisition time. Further improvements in pre-mapping of the chip, in combination with fast read-out X-ray detectors, will greatly facilitate high-throughput serial crystallography at XFELs, potentially requiring only minutes of data collection for static structure determination. This chip concept is therefore an ideal approach for precious crystalline protein samples and oversubscribed XFEL beamlines. The most significant future improvement will be the identification of spectral features or other probes of single-crystal character that are better correlated with X-ray diffraction quality so that the mapping procedure can lead to the maximum possible indexable hit rates for a given system.

6. Related literature

The following reference is cited in the Supporting Information for this article: von Stetten *et al.* (2015).

Acknowledgements

This research was supported by the Natural Sciences and Engineering Research Council of Canada (NSERC) (RJDM), the Max Planck Society (RJDM), the Canadian Institute for Advanced Research (RJDM, OPE and DIS) and the Canada Excellence Research Chair program (OPE). OPE is the Anne and Max Tanenbaum chair in Neuroscience at the University of Toronto. The research leading to these results has received funding from the People Programme (Marie Curie Actions) of the European Union's Seventh Framework Programme (FP7/2007–2013) under REA grant agreement No. 623994 (HM-W). We would like to thank the staff at Toronto Nanofabrication Centre (TNFC) for their support. Use of the Linac Coherent Light Source (LCLS), SLAC National Accelerator Laboratory is supported by the US Department of Energy, Office of Science and Office of Basic Energy Sciences under Contract No. DE-AC02-76SF00515. This work made use of user facilities at SACLA, RIKEN, Japan with the approval of the Japan Synchrotron Radiation Research Institute (JASRI) (Proposal No. 2016A8036).

References

Barends, T. R. M. *et al.* (2015). *Science*, **350**, 445–450.
Barty, A. *et al.* (2011). *Nature Photonics*, **6**, 35–40.
Barty, A., Kirian, R. A., Maia, F. R. N. C., Hantke, M., Yoon, C. H., White, T. A. & Chapman, H. (2014). *J. Appl. Cryst.* **47**, 1118–1131.
Baxter, E. L. *et al.* (2016). *Acta Cryst.* D**72**, 2–11.
Boutet, S. *et al.* (2012). *Science*, **337**, 362–364.
Chapman, H. N. *et al.* (2011). *Nature (London)*, **470**, 73–77.
Chollet, M. *et al.* (2015). *J. Synchrotron Rad.* **22**, 503–507.
Chreifi, G., Baxter, E. L., Doukov, T., Cohen, A. E., McPhillips, S. E., Song, J., Meharenna, Y. T., Soltis, S. M. & Poulos, T. L. (2016). *Proc. Natl Acad. Sci. USA*, **113**, 1226–1231.
Cohen, A. E. *et al.* (2014). *Proc. Natl Acad. Sci. USA*, **111**, 17122–17127.
Coppens, P., Pitak, M., Gembicky, M., Messerschmidt, M., Scheins, S., Benedict, J., Adachi, S., Sato, T., Nozawa, S., Ichiyanagi, K., Chollet, M. & Koshihara, S. (2009). *J. Synchrotron Rad.* **16**, 226–230.
DePonte, D. P., Weierstall, U., Schmidt, K., Warner, J., Starodub, D., Spence, J. C. H. & Doak, R. B. (2008). *J. Phys. D Appl. Phys.* **41**, 195505.
Emsley, P., Lohkamp, B., Scott, W. G. & Cowtan, K. (2010). *Acta Cryst.* D**66**, 486–501.
Ginn, H. M., Brewster, A. S., Hattne, J., Evans, G., Wagner, A., Grimes, J. M., Sauter, N. K., Sutton, G. & Stuart, D. I. (2015). *Acta Cryst.* D**71**, 1400–1410.
Ginn, H. M., Evans, G., Sauter, N. K. & Stuart, D. I. (2016). *J. Appl. Cryst.* **49**, 1065–1072.
Ginn, H. M., Messerschmidt, M., Ji, X., Zhang, H., Axford, D., Gildea, R. J., Winter, G., Brewster, A. S., Hattne, J., Wagner, A., Grimes, J. M., Evans, G., Sauter, N. K., Sutton, G. & Stuart, D. I. (2015). *Nature Commun.* **6**, 6435.

Ginn, H. M., Roedig, P., Kuo, A., Evans, G., Sauter, N. K., Ernst, O., Meents, A., Müller-Werkmeister, H., Miller, R. J. D. & Stuart, D. I. (2016). *Acta Cryst.* D**72**, 956–965.
Guha, S., Perry, S. L., Pawate, A. S. & Kenis, P. J. A. (2012). *Sens. Actuators B Chem.* **174**, 1–9.
Hirata, K. *et al.* (2014). *Nature Methods*, **11**, 734–736.
Hunter, M. S. *et al.* (2014). *Sci. Rep.* **4**, 6026.
Kabsch, W. (2010). *Acta Cryst.* D**66**, 125–132.
Keedy, D. A. *et al.* (2015). *Elife*, **4**, e07574.
Kern, J. *et al.* (2014). *Nature Commun.* **5**, 4371.
Kirchner, F. O., Lahme, S., Riedle, E. & Baum, P. (2014). *AIP Adv.* **4**, 077134.
Li, T., Quillin, M. L., Phillips, G. N. Jr & Olson, J. S. (1994). *Biochemistry*, **33**, 1433–1446.
Lyubimov, A. Y., Murray, T. D., Koehl, A., Araci, I. E., Uervirojnangkoorn, M., Zeldin, O. B., Cohen, A. E., Soltis, S. M., Baxter, E. L., Brewster, A. S., Sauter, N. K., Brunger, A. T. & Berger, J. M. (2015). *Acta Cryst.* D**71**, 928–940.
Mariani, V., Morgan, A., Yoon, C. H., Lane, T. J., White, T. A., O'Grady, C., Kuhn, M., Aplin, S., Koglin, J., Barty, A. & Chapman, H. N. (2016). *J. Appl. Cryst.* **49**, 1073–1080.
McCoy, A. J., Grosse-Kunstleve, R. W., Adams, P. D., Winn, M. D., Storoni, L. C. & Read, R. J. (2007). *J. Appl. Cryst.* **40**, 658–674.
Mueller, C. *et al.* (2015). *Struct. Dyn.* **2**, 054302.
Murray, T. D., Lyubimov, A. Y., Ogata, C. M., Vo, H., Uervirojnangkoorn, M., Brunger, A. T. & Berger, J. M. (2015). *Acta Cryst.* D**71**, 1987–1997.
Murshudov, G. N., Skubák, P., Lebedev, A. A., Pannu, N. S., Steiner, R. A., Nicholls, R. A., Winn, M. D., Long, F. & Vagin, A. A. (2011). *Acta Cryst.* D**67**, 355–367.
Owen, R. L., Yorke, B. A., Gowdy, J. A. & Pearson, A. R. (2011). *J. Synchrotron Rad.* **18**, 367–373.
Pearson, A. R., Pahl, R., Kovaleva, E. G., Davidson, V. L. & Wilmot, C. M. (2007). *J. Synchrotron Rad.* **14**, 92–98.
Roedig, P., Duman, R., Sanchez-Weatherby, J., Vartiainen, I., Burkhardt, A., Warmer, M., David, C., Wagner, A. & Meents, A. (2016). *J. Appl. Cryst.* **49**, 968–975.
Roedig, P., Vartiainen, I., Duman, R., Panneerselvam, S., Stübe, N., Lorbeer, O., Warmer, M., Sutton, G., Stuart, D. I., Weckert, E., David, C., Wagner, A. & Meents, A. (2015). *Sci. Rep.* **5**, 10451.
Roessler, C. G. *et al.* (2016). *Structure*, **24**, 631–640.
Seidel, H. (1990). *J. Electrochem. Soc.* **137**, 3612–3626.
Sherrell, D. A., Foster, A. J., Hudson, L., Nutter, B., O'Hea, J., Nelson, S., Paré-Labrosse, O., Oghbaey, S., Miller, R. J. D. & Owen, R. L. (2015). *J. Synchrotron Rad.* **22**, 1372–1378.
Sierra, R. G. *et al.* (2012). *Acta Cryst.* D**68**, 1584–1587.
Springer, B. A. & Sligar, S. G. (1987). *Proc. Natl Acad. Sci. USA*, **84**, 8961–8965.
Stetten, D. von, Giraud, T., Carpentier, P., Sever, F., Terrien, M., Dobias, F., Juers, D. H., Flot, D., Mueller-Dieckmann, C., Leonard, G. A., de Sanctis, D. & Royant, A. (2015). *Acta Cryst.* D**71**, 15–26.
Sugahara, M. *et al.* (2015). *Nature Methods*, **12**, 61–63.
Tenboer, J. *et al.* (2014). *Science*, **346**, 1242–1246.
Waterman, D. G., Winter, G., Gildea, R. J., Parkhurst, J. M., Brewster, A. S., Sauter, N. K. & Evans, G. (2016). *Acta Cryst.* D**72**, 558–575.
Weierstall, U. *et al.* (2014). *Nature Commun.* **5**, 3309.
White, T. A., Kirian, R. A., Martin, A. V., Aquila, A., Nass, K., Barty, A. & Chapman, H. N. (2012). *J. Appl. Cryst.* **45**, 335–341.
Winn, M. D. *et al.* (2011). *Acta Cryst.* D**67**, 235–242.
Yang, F. & Phillips, G. N. Jr (1996). *J. Mol. Biol.* **256**, 762–774.
Zarrine-Afsar, A., Barends, T. R. M., Müller, C., Fuchs, M. R., Lomb, L., Schlichting, I. & Miller, R. J. D. (2012). *Acta Cryst.* D**68**, 321–323.
Zeldin, O. B., Gerstel, M. & Garman, E. F. (2013). *J. Appl. Cryst.* **46**, 1225–1230.
Zhou, Q. *et al.* (2015). *Nature (London)*, **525**, 62–67.